Photoacoustic Multispectral Elastography Based on the Photoacoustic Oscillation Effect for Microelastomers in Deep Tissue

Yang Liu, Chao Tao,* and Xiaojun Liu†

Ministry-of-Education Key Lab of Modern Acoustics, Department of Physics, Collaborative Innovation Center of Advanced Microstructure, Nanjing University, Nanjing 210093, People's Republic of China

(Received 16 February 2023; revised 22 May 2023; accepted 17 July 2023; published 14 August 2023)

The detection of microelastomers in deep tissue has significant biomedical value. However, elastography of microelastomers is still limited to superficial tissues. Here, we propose photoacoustic multiacoustic spectral elastography based on the photoacoustic oscillation effect. After illumination with a pulsed laser, a light-absorbing elastomer vibrates and emits damped ultrasound waves, i.e., eigenvibro signals, in a short time. The eigenvibro signals contain elastic information. Our proposed method utilizes a causal damped wavelet to enhance and decompose the eigenvibro signals. Each wavelet basis corresponds to a distinct frequency, enabling the wavelet transformation of the photoacoustic signals and their synthesis to generate frequency-specific images. These individual images collectively form multispectral images, effectively displaying elastic features at their respective frequencies. Then, the elastogram of microelastomers in the region of interest is reconstructed and includes the intensity image, peak-frequency image, quality-factor image, and elasticity-to-viscosity ratio image. Both numerical simulations and phantom experiments validate the suitability of our proposed method, even with interference from inelastic optical absorbers. Our study has potential biomedical value for the assessment of diseases resulting from the development of microelastomers.

DOI: 10.1103/PhysRevApplied.20.024035

I. INTRODUCTION

Photoacoustic tomography is a hybrid imaging modality that combines the rich contrast of optical imaging and the high spatial resolution of ultrasonic imaging in deep tissue [1–5]. It has shown great potential in biomedical research and clinical applications, such as microvascular imaging [6–8], tumor diagnosis [9,10], osteoarthritis assessment [11], and drug-delivery monitoring [12].

The elasticity of a biological microstructure is closely related to pathological states [13–21]. Elastography is any class of medical imaging modalities that map the elastic properties and stiffness of soft tissue [22–28]. Elastography based on prominent imaging techniques, including ultrasound elastography, magnetic resonance elastography, and optical coherence elastography, has been popular in the last decade. Photoacoustic imaging is also applied to measure the elastic properties of biological tissue [29–36]. For example, quantitative photoacoustic elastography was applied to quantify the Young's modulus of human skeletal muscle *in vivo* [29,30]. However, these methods face challenges when dealing with irregular objects due to the requirement of applying uniform pressure to the target being measured [29,30]. Another approach involves the development of photoacoustic viscoelasticity imaging, which establishes a relationship between the phase delay of photoacoustic signals and the viscoelasticity of biological tissue [31]. All-optical noncontact photoacoustic elastography, on the other hand, determines the bulk elastic modulus of tissue by analyzing the rising time of echo, without the need for physical contact [32,33]. Additionally, the utilization of a picosecond optoacoustic technique enables imaging with submicron resolution of complex longitudinal moduli [34–36]. However, these techniques are limited to measuring the superficial elastic properties of tissues, as they rely on objective lens or pump probes [31–36]. These studies indicated that photoacoustic imaging could provide feasible methods to measure the elasticity of biological tissue.

Recently, a photoacoustic oscillation phenomenon was observed when an elastomer in biological tissue was exposed to pulsed laser illumination [37–39]. This phenomenon provides an alternative possibility to achieve elastography for tissue. When a laser pulse illuminates a light-absorbing elastomer, due to the absorption of laser energy, the laser causes the optical absorber to expand and emit broadband ultrasound waves into the surrounding medium, which is the photoacoustic effect. Our name for wideband ultrasound waves is laser-forced signals. When a pulse laser ceases, the elastomer keeps vibrating and emits ultrasound waves for a short time due to inertia.

*taochao@nju.edu.cn
†liuxiaojun@nju.edu.cn

Typically, this signal is observed as a weakly damped transient wave, and our name for this signal is an eigenvibro signal, since it is emitted by the eigenvibration of an elastomer. The eigenvibro signal is closely related to mechanical properties such as elasticity and viscosity. Therefore, the elastic misconstruction can be reconstructed from the detected eigenvibro signals. The photoacoustic oscillation phenomenon can facilitate insights into tissue elasticities.

Several studies have been performed to image the elastic properties of biological tissue by using the photoacoustic oscillation effect. For example, by analyzing the peak ratio between the first peak and the second peak of the photoacoustic signal, researchers obtained images of the elastic properties of superficial tissues via point-by-point scanning [39]. Recently, we proposed a photoacoustic holography algorithm to extract microelastomers from bright backgrounds [40].

However, there are still many challenges in imaging microelastomers in deep tissue using the photoacoustic oscillation effect. Eigenvibro signals are usually very weak and sustained for a short time, and they are often mixed with laser-forced signals. Living tissue always contains strong optical absorbers, such as blood vessels. These absorbers generate intense laser-forced signals and overwhelm the weak eigenvibro signals. Therefore, conventional methods have difficulty in extracting the eigenvibro signals from the photoacoustic signals. Elastography based on the photoacoustic oscillation effect is still limited to imaging superficial tissue or elastomers with strong eigenvibro signals. Moreover, it can rely on prior information related to the spectrum of photoacoustic signals.

Here, we propose a method based on the photoacoustic oscillation effect to image microelastomers in deep tissue. In our method, we initially enhance and decompose eigenvibro signals by using a causal damped wavelet. Then, we reconstruct a series of multispectral images. Each image corresponds to a characteristic frequency. Finally, we extract an elastogram of microelastomers in the region of interest. Both numerical simulations and phantom experiments are performed to validate our proposed elastography method.

II. IMAGING THEORY

Under the illumination of a pulse laser, the elastomers absorb part of the energy and convert it into heat. Nonionizing laser pulses force elastomer expansion and thermal stress source, q_{force}, generation. Then, the transient thermoelastic expansion can lead to the vibration of the elastomers. The viscosity of tissue governs the rate of the vibration decay: greater viscosity leads to faster vibration decay, causing the vibration to cease after a few cycles. Assuming spatial variations in the bulk elastic moduli (E) and viscous moduli (η) of the tissue, along with independent vibrations of each elastomer, the laser-induced vibration of the elastomers can be described by a modified Kelvin-Voigt model, as follows [41]:

$$m\frac{\partial^2 u}{\partial t^2}+\eta\frac{\partial u}{\partial t}+Eu-q_{\text{force}}(\mathbf{r},t)=0, \tag{1}$$

where m is the mass of the elastomer, E is the elastic modulus, η is the viscous modulus, $q_{\text{force}}(\mathbf{r},t)=\alpha(\mathbf{r})\partial I(t)/\partial t$ is a thermal stress source due to laser absorption, I is a function of the temporal profile of the laser pulse, α is a coefficient related to light absorption and thermal expansion properties, and $\mathbf{r}$ is the spatial coordinate of the light absorbers. Then, the oscillation displacement, u, excited by q_{force} can be calculated from Eq. (1) as follows:

$$u(\mathbf{r},t)=\int_0^t q_{\text{force}}(\mathbf{r},\tau)\times g(t-\tau)d\tau, \tag{2}$$

with the use of the following relationship:

$$g(t)=\frac{\exp(-(\omega_0/2Q)t)\sin\left(\omega_0\sqrt{1-1/(4Q^2)}t\right)}{m\omega_0\sqrt{1-1/(4Q^2)}}, \tag{3}$$

where $Q=(mE)^{1/2}/\eta$ is the quality factor and $\omega_0=(E/m)^{1/2}$ is the intrinsic frequency.

The vibration of elastomers continues irradiating ultrasound waves to the surrounding media. Therefore, the elastomers can be considered a sound source, q_{vibro}, which can be related to the displacement, u, by $q_{\text{vibro}}(\mathbf{r},t)\sim\rho c\partial u(\mathbf{r},t)/\partial t$, where ρ and c are the density and speed of sound in the surrounding media, respectively.

Using an ultrasound transducer, the ultrasound waves generated by the elastomers can be detected at $\mathbf{r}_d$, which is recorded as $p(\mathbf{r}_d,t)$. In a homogeneous medium, $p(\mathbf{r}_d,t)$ can be expressed as follows:

$$p(\mathbf{r}_d,t)=\frac{1}{4\pi}\iiint_V q\left(\mathbf{r},t-\frac{||\mathbf{r}_d-\mathbf{r}||}{c}\right)\frac{dr}{||\mathbf{r}_d-\mathbf{r}||}. \tag{4}$$

where $\mathbf{r}_d$ is the coordinate of the detection position, c is the speed of sound, and $q(\mathbf{r},t)$ is the pressure source at $\mathbf{r}$.

Clearly, the pressure source, $q(\mathbf{r},\text{t})$, is a combination of the laser-force vibration, q_{force}, and elastomer eigenvibration, q_{vibro}, as follows:

$$q(\mathbf{r},t)=q_{\text{force}}(\mathbf{r},t)+q_{\text{vibro}}(\mathbf{r},t). \tag{5}$$

Therefore, the detected signal, $p(\mathbf{r}_d,t)$, also includes two components, $p_{\text{force}}(\mathbf{r}_d,t)$ and $p_{\text{vibro}}(\mathbf{r}_d,t)$, where p_{force} and p_{vibro} come from q_{force} and q_{vibro}, respectively. $p(\mathbf{r}_d,t)$ contains not only light-absorption properties (q_{force}) of the elastomer but also elastic properties (q_{vibro}) of the source. Both the optical absorption image and the elastic image of the sound sources can be reconstructed from the detected signals, $p(\mathbf{r}_d,t)$. This is the theoretical basis of photoacoustic multiacoustic spectral elastography discussed in the following.

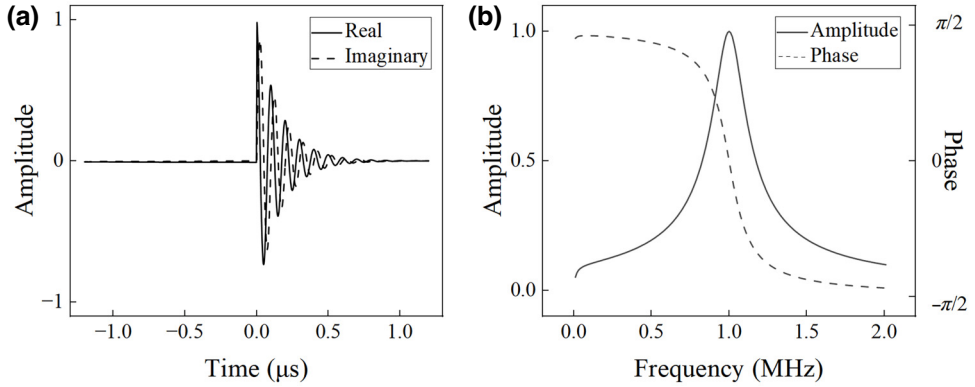

FIG. 1. Temporal and spectral representations of the mother wavelet ($\omega_0 = 1$ MHz). (a) Temporal representations, the solid line and the dotted line correspond to the real part and the imaginary part of the mother wavelet, respectively. (b) Spectral representations, the solid line and the dotted line describe the amplitude and the phase of mother wavelet ψ_0, respectively.

A. Enhancement and decomposition of the eigenvibro signals by using a causal damped wavelet

Generally, the eigenvibro signal, p_{vibro}, induced by a pulsed laser is very weak in comparison with the laser-forced component, p_{force}. Considering the natural time-frequency characteristics of the eigenvibro signals induced by the laser, as shown in Eq. (2), we use a causal damped wavelet to decompose the detected signals and enhance the eigenvibro components. The mother wavelet ψ_0 of the causal damped wavelet is given by [42]

$$\psi_0(t) = H(t)\exp\left(\left(-\frac{\omega_0}{2Q} + i\omega_0\right)t\right) + \frac{\omega_\Delta}{\omega_0}H(-t)\exp\left(\left(\frac{\omega_\Delta}{2Q} - i\omega_\Delta\right)t\right), \quad (6)$$

where H refers to the Heaviside step function, ω_0 is the eigenvibration frequency, Q is the quality factor, and ω_Δ is the spectral resolution of the wavelet. Generally, ω_Δ is much lower than ω_0.

In the spectral domain, the mother wavelet $\Psi_0(\omega)$ is expressed as follows:

$$\Psi_0(\omega) = \frac{1}{(\omega_0/2Q) + i(\omega - \omega_0)} - \frac{\omega_\Delta/\omega_0}{(\omega_\Delta/2Q) - i(\omega_\Delta + \omega)}. \quad (7)$$

Figure 1(a) shows the waveform of the mother wavelet, which is the damped transient wave. From Fig. 1(b), we can observe that the phase of the mother wavelet ψ_0 is zero, while the amplitude reaches its maximum at an intrinsic frequency, ω_0, of 1.0 MHz. The phase also demonstrates a linear trend around its intrinsic frequency, ω_0, of 1.0 MHz.

Figure 2 compares the mother wavelet with the photoacoustic signals generated by the elastomer in terms of its waveform and spectrum. The mother wavelet effectively matches the eigenvibro signal rather than the laser-forced signal.

Applying a scale factor, a, to the mother wavelet, we can obtain a wavelet basis series, as follows:

$$\psi_a(t) = \frac{1}{\sqrt{a}}\psi_0\left(\frac{t}{a}\right), \quad (8)$$

$$= \frac{1}{\sqrt{a}}H(t)e^{(-(\omega_0/2Q)+i\omega_0)(t/a)} + \frac{\omega_\Delta}{\sqrt{a}\omega_0}H(-t)e^{((\omega_\Delta/2Q)-i\omega_\Delta)(t/a)}. \quad (9)$$

Each wavelet basis, $\psi_a(t)$, corresponds to an angular frequency of $\omega_a = \omega_0/a$.

Correlating the detected signal, $p(\mathbf{r}_d,t)$, with the child wavelet basis, $\psi_a(t)$, we can decompose $p(\mathbf{r}_d,t)$ signals into a series of components $s(\mathbf{r}_d,t,\omega_a)$, as follows:

$$s(\mathbf{r}_d, t, \omega_a) = \int_{-\infty}^{+\infty} p(\mathbf{r}_d, \tau) \times \psi_a(\tau - t)d\tau. \quad (10)$$

Each component $s(\mathbf{r}_d,t,\omega_a)$ corresponds to a frequency of ω_a. As the eigenvibro signal appears and its frequency coincides with the child wavelet basis, $s(\mathbf{r}_d,t,\omega_a)$ has high amplitude; otherwise, its magnitude is low. Since the causal damped wavelet has similar time-frequency characteristics to the transient vibro components in the photoacoustic signals, the causal damped wavelet can detect and enhance the eigenvibro components.

B. Reconstruction of the multispectral images from the eigenvibro signals

The child wavelet, $\psi_a(t)$, has a linear phase around the intrinsic frequency, ω_a. The phase of $s(\mathbf{r}_d,t,\omega_a)$ is consistent with that of $p(\mathbf{r}_d,t)$ around the intrinsic frequency, ω_a,

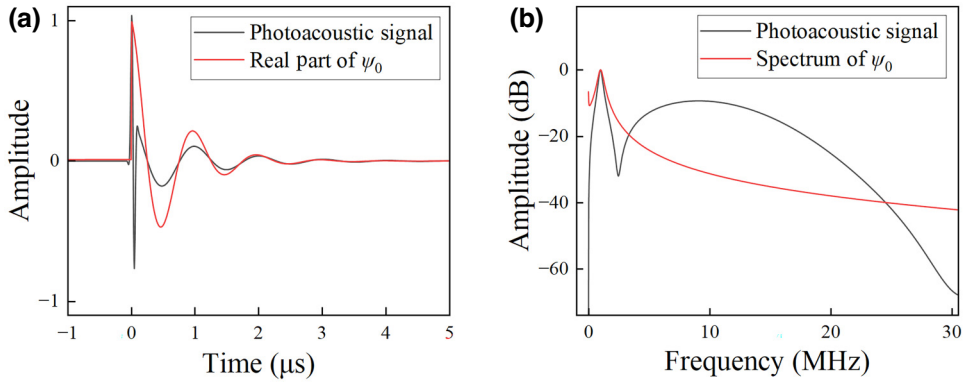

FIG. 2. Temporal and spectral representations of the mother wavelet ψ_0 and the photoacoustic signal from microelastomers under the illumination of a pulse laser. (a) Temporal representations: the black line and the red line correspond to the photoacoustic signal and the real part of the mother wavelet ψ_0, respectively. (b) Spectral representations: the black line and the red line correspond to the photoacoustic signal and the real part of the mother wavelet ψ_0, respectively.

and not consistent away from ω_a. Therefore, series images, $A(\mathbf{r},\omega_a)$, can be reconstructed from each decomposed signal, $s(\mathbf{r}_d,t,\omega_a)$, through the delay-and-sum method [43–45], as follows:

$$A(\mathbf{r},\omega_a)=\int_{\Omega_0} s(\mathbf{r}_d,t,\omega_a)\frac{d\Omega}{\Omega_0}|_{t=\frac{||\mathbf{r}-\mathbf{r}_d||_2}{c}}, \tag{11}$$

where $d\Omega$ is the solid angle for the detection element at $\mathbf{r}_d$ and is defined as follows:

$$d\Omega=\frac{dS}{||\mathbf{r}-\mathbf{r}_d||^2}\frac{\mathrm{n}_s(\mathbf{r})\cdot(\mathbf{r}-\mathbf{r}_d)}{||\mathbf{r}-\mathbf{r}_d||}, \tag{12}$$

where $\mathbf{r}$ represents the coordinate of the pixels in the image, dS is the surface area of the detection element, and $\mathbf{n}_s(\mathbf{r})$ is the ingoing normal vector. The total solid angle is denoted as Ω_0.

For a two-dimensional situation, the integration of Eq. (12) is provided as follows:

$$A(x,y,\omega_a)=\sum_i \frac{s({x_d}^i,{y_d}^i,t,\omega_a)}{\sqrt{(x-{x_d}^i)^2+(y-{y_d}^i)^2}} |_{t=\sqrt{(x-x_d^i)^2+(y-y_d^i)^2}/c}, \tag{13}$$

where $({x_d}^i,{y_d}^i)$ is the coordinate of the ith detection point.

Repeating the above process for each decomposed signal, $s(x_d,y_d,t,\omega_a)$, we can obtain an image sequence, $A(x,y,\omega_a)$. Each image corresponds to frequency ω_a. These multispectral images show feature images of the region of interest at their corresponding frequencies. The elastomers can be highlighted in the images, which correspond to the eigenvibro frequencies of microelastomers.

C. Extraction of the elastogram from multispectral images

In the third step, we extract the elastogram from multispectral images. Both microelastomers and inelastic optical absorbers can be observed in these multispectral images. In addition, they have different features in these multispectral images due to time-frequency characteristic differences of the p_{forced} component and p_{vibro} component. The laser-forced component, p_{forced}, in a photoacoustic signal has an extremely broad bandwidth, resulting from the narrow pulse width of the nanosecond laser. In contrast, the eigenvibro component has a narrow bandwidth because it is generated from a damped free-oscillation process.

Their difference is reflected by the multispectral images. For any given position (x, y) in multispectral images, the intensity of a pixel, $A(x, y, \omega_a)$, is a function of ω_a. The same pixel in each multispectral image constructs a curve, which is similar to a spectral curve. These curves are analogous to the optical spectrum, but they reflect the vibrational properties of the imaging targets. All spectral curves have a wide and flat base due to the laser-forced components. For microelastomers, a narrow peak is located on the flat base, corresponding to the eigenvibro components. Therefore, by removing the wide and flat base (laser-forced components) from the multispectral images, we can extract the elastic feature of the region of interest.

Since the laser-forced components dominate the energy of the detected photoacoustic signals, their spectral characteristics can be approximately estimated as follows:

$$I_{\text{force}}(\omega_a)=\frac{1}{S}\iint_{\text{ROI}} A(x,y,\omega_a)A^*(x,y,\omega_a)dxdy, \tag{14}$$

where S is the area of the pressure source in the region of interest and A^* is the complex conjugate of A. Then, removing the laser-forced components from the image

sequence, $A(x,y,\omega_a)$, we have the following result:

$$I_{\text{vibro}}(x,y,\omega_a) = A(x,y,\omega_a)A^*(x,y,\omega_a) - I_{\text{force}}(\omega_a), \tag{15}$$

where $I_{\text{vibro}}(x,y,\omega_a)$ represents the image that reflects the elastic characteristics corresponding to ω_a.

Finally, four images are extracted from the $I_{\text{vibro}}(x,y,\omega_a)$ image series. The first one is a total-intensity image, $I(x,y)$, of the eigenvibration energy, as follows:

$$I(x,y) = \sum\nolimits_{\omega_a} I_{\text{vibro}}(x,y,\omega_a). \tag{16}$$

The second image is a peak-frequency image, $\omega_P(x,y)$, the pixel intensity, $\omega_P(x,y)$, of which is the frequency value maximizing $I_{\text{vibro}}(x,y,\omega_a)$, as follows:

$$\omega_P(x,y) = \arg\max_{\omega_a} I_{\text{vibro}}(x,y,\omega_a). \tag{17}$$

The causal damped wavelet basis depends on two parameters: the intrinsic frequency, ω_a, and the quality factor, Q. After setting the peak frequency, we extract the quality-factor image, $Q_P(x,y)$, as follows:

$$Q_P(x,y) = \arg\max_{Q} I_{\text{vibro}}(x,y,\omega_p). \tag{18}$$

The quality factor, $Q=(mE)^{1/2}/\eta$, and the intrinsic frequency, $\omega_0=(E/m)^{1/2}$, have a product of E/η, which is the ratio of the bulk elastic modulus and viscous modulus of the microstructure [46,47]. Thus, we can define the elasticity-to-viscosity ratio image, $R_P(x,y)$, as follows:

$$R_P(x,y) = \omega_P(x,y)Q_P(x,y). \tag{19}$$

The total-intensity image, $I(x,y)$; the peak-frequency image, $\omega_P(x,y)$; the quality-factor image, $Q_P(x,y)$; and the elasticity-to-viscosity ratio image, $R_P(x,y)$, produce the elastogram of the region of interest. $I(x,y)$ shows the total intensity of the eigenvibration energy within the region of interest, and $\omega_P(x,y)$ shows the peak-frequency information in that region. $Q_P(x,y)$ serves as an indicator of the attenuation characteristics of the eigenvibration, providing information regarding how quickly the eigenvibration energy decays in the region of interest. $R_P(x,y)$ estimates the ratio of the bulk elastic modulus to the viscous modulus within the imaging area. Pixels with high-intensity values on the intensity image, $I(x,y)$, indicate the location of microelastomers, where the peak frequency is generally the eigenvibration frequency of these microelastomers. As a result, these four images collectively show the elastogram of the tissue, providing comprehensive information about its elastic properties.

III. NUMERICAL STUDIES AND RESULTS

Numerical studies are performed to explain the imaging process and verify the feasibility of our proposed method. Signal generation and propagation are simulated by using the numerical integral method and the *k*-space pseudospectral method [48,49] based on the MATLAB toolbox.

A. Image of the elastic point source

In the first numerical experiment, we image nine optical absorbers with different elastic properties.

The simulation of signal generation and propagation is based on a homogeneous medium with a speed of sound of 1500 m/s. The simulation area is a square area (52×52 mm^2), as shown in Fig. 3(a). Signals are recorded by a 256-channel ring array with a diameter of 50 mm, as shown by the black dashed line in Fig. 3(a). Points N1–N8 in Fig. 3(b) represent the eight normal point optical absorbers. In this simulation, microelastomer E1 has a density of 1 g/cm^3, an elastic modulus of 0.395 GPa, and a viscosity modulus of 31.4 Pa s, which corresponds to an eigenvibration with a frequency of 1 MHz and quality factor of 3. When exposed to laser irradiation, points N1–N8 emit only the laser-forced signals; however, point E1 also generates a weak eigenvibro component with a central frequency of 1 MHz and a quality factor of 3, as shown in Figs. 3(c) and 3(d).

Figure 4(a) shows one typical $p(x_d,y_d,t)$ signal detected by the transducer at detection point D, as shown in Fig. 3(a). Since point N1 is the signal source closest to detection point D, the first signal in Fig. 4(a) is propagated from point N1. In the same way, the last signal in Fig. 4(a) is propagated from E1. The first eight signals contain only the laser-forced components, and the last signal contains the laser-forced signal and the eigenvibro signal. Correlating the typical signal with the child wavelet basis, we decompose the signal into a series of components, $s(x_d,y_d,t,\omega_a)$, as shown in Figs. 4(b)–4(f). The component from the eigenvibro signal is enhanced by the wavelet transform and reaches its maximum at an intrinsic frequency, ω_0, of 1 MHz, as shown in Fig. 4(c). Moreover, the components from laser-forced signals are suppressed.

The eigenvibro signal from a microelastomer appears later than the laser-forced signal. In Fig. 4(c), M1 contains the component from N1's laser-forced signal, but M2 does not. Additionally, M3 contains the component from E1's laser-forced signal, and M4 contains the component from E1's eigenvibro signal. Furthermore, the child wavelet, $\psi_a(t)$, has a linear phase around intrinsic frequency ω_a, and the energy of the eigenvibro signals is also concentrated around intrinsic frequency ω_a, whereas the energy of the laser-forced signals is distributed over a wide frequency range. After the wavelet transform, components $s(x_d,y_d,t,\omega_a)$ from the eigenvibro signals

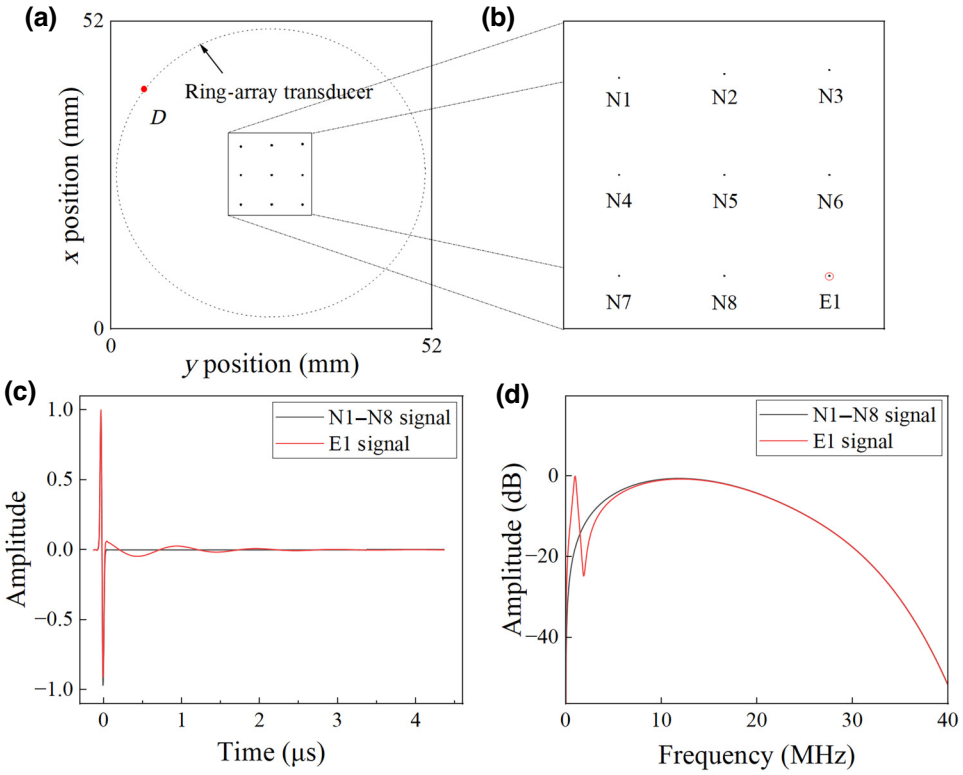

FIG. 3. Simulation of signal generation and propagation from nine point targets with different elasticity. (a) Nine point-signal sources and ring-array transducer. (b) N1–N8 are eight normal point optical absorbers with low elasticity and E1 is an elastomer. (c) Waveforms of emitted signals; black line is the waveform of the signal emitted by the eight normal point optical absorbers and only contains a laser-forced signal; red line is the waveform of the signal emitted by the elastomer, which contains both the laser-forced signal and the eigenvibro signal with a central frequency of 1 MHz and a quality factor of 3. (d) Spectra of the signals from N1-N8 and the signal from E1.

maintain a linear phase and satisfy spatial coherence at an intrinsic frequency of ω_a, but components $s(x_d,y_d,t,\omega_a)$ from laser-forced signals do not satisfy spatial coherence. Therefore, using the decomposed signal, $s(x_d,y_d,t,\omega_a)$, we can reconstruct the images that reflect the elastic features of these point sources.

Based on the following comparison, Fig. 5(a) shows a conventional photoacoustic image reconstructed from the detected signals by using a delay-and-sum algorithm; the image clearly shows the locations of the four sources, N5, N6, N8, and E1. However, elastomer E1 is the same as the other normal sources. The abnormal elasticity target cannot be obtained via this conventional photoacoustic image. Figure 5(b) shows the image reconstructed from $s(\mathbf{r}_d,t,\omega_a)$ with $\omega_a = 1$ MHz; since the eigenvibro signals emitted from elastomers are enhanced by the causal damped wavelet transform, point elastomer E1 is emphasized in comparison with the other normal sources.

Figure 5(c) plots the pixel intensity of each image as a function of ω_a, where the red curve, black curve, and blue curve correspond to the imaging pixels of elastomer E1, normal source N1, and an average intensity of the whole image, respectively; all curves have a wide and flat base, corresponding to the laser-forced signals. For elastomer E1, a narrow peak at a frequency of 1 MHz is located on the flat base, corresponding to the eigenvibro signal. Therefore, by removing the wide and flat base from the multispectral images, we can extract the elastic feature of the region of interest. Figure 5(d) shows the total-intensity image, $I(x,y)$, after extracting the elastic feature of the region of interest; only elastomer E1 is visible, and other normal sources are not observed. Figures 5(e) and 5(f) show the peak-frequency image, $\omega_p(x,y)$, and quality-factor image, $Q_p(x,y)$, of the region of interest. We use the hue-saturation-value (HSV) color space to encode the peak frequency (quality factor) and intensity in the region of interest. The hue is encoded using peak-frequency (quality-factor) information. The intensity is mapped to the value component in HSV. This creates Figs. 5(e) and 5(f), where color is determined by peak frequency (quality factor) and brightness by intensity; the peak frequency of the eigenvibration for elastomer E1 is approximately 1 MHz, with an associated quality factor of approximately 3. Figures 5(e) and 5(f) collectively produce the elastogram of the region of interest. Additionally, we

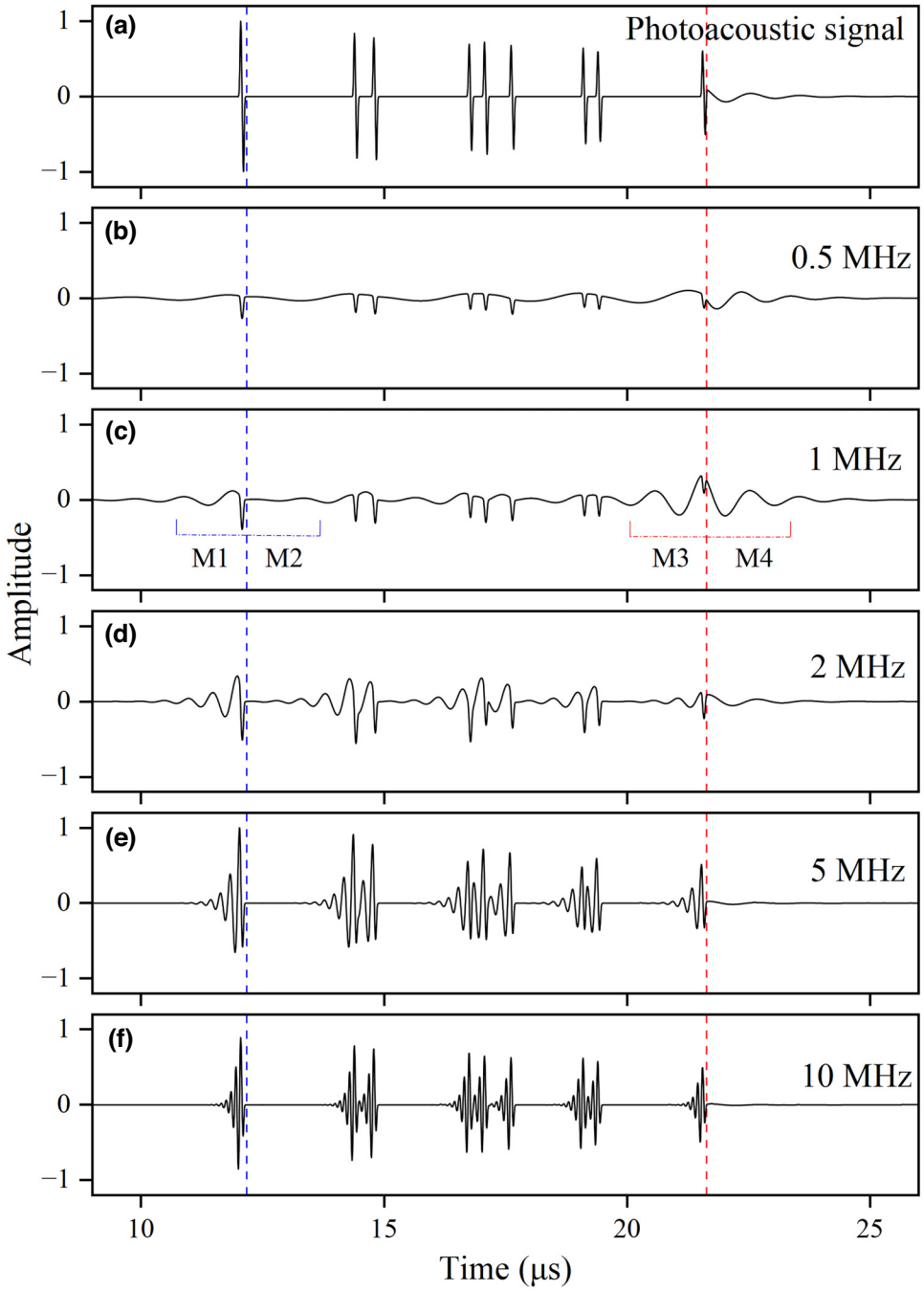

FIG. 4. Photoacoustic signals, $p(x_d,y_d,t)$, detected at D and a series of components, $s(x_d,y_d,t,\omega_a)$, at different frequencies via the wavelet transform. (a) Photoacoustic signal, $p(x_d,y_d,t)$, detected at detector D. (b)–(f) Decomposed signals, $s(x_d,y_d,t,\omega_a)$, after causal damped wavelet transform with frequencies, ω_a, of 0.5, 1, 2, 5, and 10 MHz.

conduct a series of simulations by varying the frequency or quality factor of E1. In Fig. 5(g), we present the estimated frequency of E1, while keeping the quality factor fixed at 3 and varying the frequency from 0.5 to 9 MHz. Furthermore, in Fig. 5(h), we showcase the estimated quality factor of E1 with a fixed frequency of 1 MHz, while varying the quality factor from 0.5 to 9. These simulations provide evidence that our proposed method accurately estimates the vibration frequency and quality factor of microelastomers.

B. Image of the elastic part in the blood-vessel network

In the second numerical simulation, we image the abnormal elastic region in the blood vessel network to verify our proposed method in complex situations.

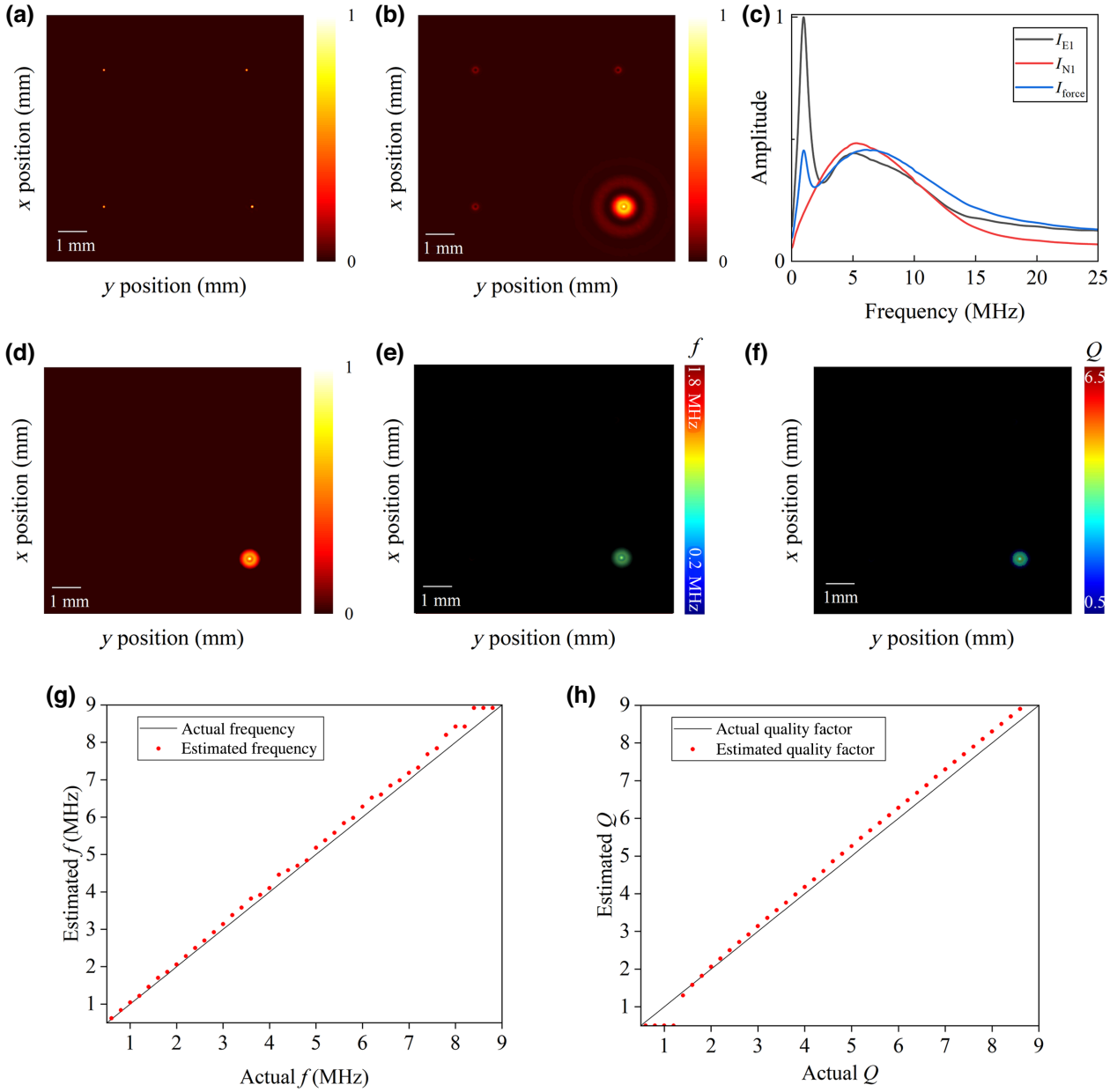

FIG. 5. Images of the elastic point source. (a) Reconstructed image using the delay-and-sum algorithm. (b) Reconstructed image from signals $s(x_d,y_d,t,\omega_a)$ with frequency $\omega_a = 1$ MHz. (c) Pixel intensity's spectral characteristic at point E1, point N1, and I_{force}. (d) Intensity image, $I(x,y)$, showing the elastic feature of the nine point sources after extracting the intensity image, $I(x,y)$, from the multispectral images. (e) Peak-frequency image, $\omega_p(x,y)$, encoded using HSV color space (hue, peak frequency; value, intensity). (f) Quality-factor image, $Q_p(x,y)$, encoded using HSV color space (hue, quality factor; value, intensity). (g) Estimated frequency of E1 with a fixed quality factor of 3 and varying frequency ranging from 0.5 to 9 MHz. (h) Estimated quality factor of E1 with a fixed frequency of 1 MHz and varying quality factor ranging from 0.5 to 9.

The medium is also homogeneous with a speed of sound of 1500 m/s. The simulation area is a square area (52×52 mm^2), as shown in Fig. 6(a). Signals are recorded by a 256-channel ring array with a diameter of 50 mm, as shown by the black dashed line. The gray part in Fig. 6(a) represents inelastic light absorbers, such as the blood-vessel network. The red and blue segments represent two regions with high elasticity, which mimic pathological tissues in blood vessels. The red microelastomer on the left has a density of 1 g/cm^3, an elastic modulus of 0.253 GPa, and a viscosity modulus of 16.8 Pa s, which correspond to a vibration with a frequency of 0.8 MHz, quality factor of 3, and elasticity-to-viscosity ratio of 15.1 μs^{-1}. Alternatively, the blue microelastomer on the right has a density of 1 g/cm^3, elastic modulus of 0.568 GPa, and viscosity modulus of 37.7 Pa s, which corresponds to a vibration with a

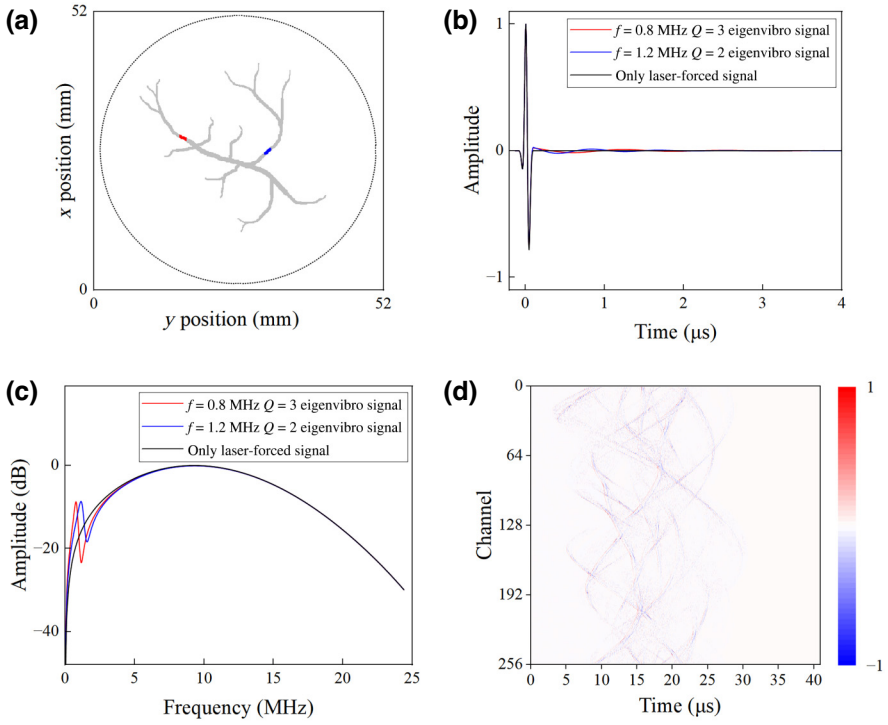

FIG. 6. Numerical simulation of blood-vessel network. (a) Diagram of blood-vessel network and ring-array transducer. (b) Signals from various parts of the blood vessel. Gray line, signal only containing laser-forced components emitted by the gray part in the vessel net; red line, signal containing an eigenvibro component with a central frequency of 0.8 MHz and a quality factor of 3 emitted by the red segment; blue line, signal containing an eigenvibro component with a central frequency of 1.2 MHz and a quality factor of 2 emitted by the blue segment. (c) Spectra of the signals. (d) Waveform of the 256-channel simulated signals.

frequency of 1.2 MHz, quality factor of 2, and elasticity-to-viscosity ratio of 15.1 μs^{-1}. The signal emitted by the gray part is assumed to contain only the laser-forced signal, as shown by the gray line in Fig. 6(b). The signals from the red and blue segments contain weak eigenvibro components with central frequencies of 0.8 and 1.2 MHz and quality factors of 3 and 2, respectively, as shown by the red line and blue line in Fig. 6(b). Figure 6(c) shows the spectrum of these signals; the amplitude of the eigenvibro components in the signals is much weaker than that of the laser-forced components. Figure 6(d) shows the waveform of the 256-channel simulated signals. Because of the irregularity of the blood-vessel network, the waveform of the detected photoacoustic signals is very complex, as shown in Fig. 6(d). Blood vessels generate strong laser-forced components, which completely overwhelm the eigenvibro components in the time and frequency domains.

Figure 7 shows the image sequence reconstructed from $s(\mathbf{r}_d,t,\omega_a)$. The two elastomers have different intensities in the nine images, indicating that the two elastomers have different elastic characteristics. In Fig. 7(d), frequency ω_a is 0.8 MHz. The strongest intensity in this image corresponds to the left elastomer [red region in Fig. 6(a)]. However, frequency ω_a in Fig. 7(f) is 1.2 MHz. The right elastomer [blue region in Fig. 6(a)] has the highest intensity in this image. The intensity of the elastomers significantly decreases in the other images, the frequencies, ω_a, of which deviate from the eigenfrequency. The image sequence shows the elastic features of the targets over a wide frequency range.

Figure 8 shows the final elastogram of the blood-vessel network. Considering the following comparison, Fig. 8(a) shows a conventional photoacoustic image reconstructed from the detected signals by using the delay-and-sum algorithm; the image clearly shows the structure of the blood-vessel network. However, the pathological region is the same as the other part of the blood vessel. The abnormal elasticity region cannot be observed in this conventional photoacoustic image. Figure 8(b) shows the total-intensity image, $I(x,y)$, reconstructed from the multispectral images in Fig. 7 using our proposed method [Eqs. (14) and (15)]. Figures 8(c)–8(e) presents the peak-frequency image, the quality-factor image, and the elasticity-to-viscosity ratio image of the blood-vessel network, respectively; these are derived from multispectral images. Different colors represent different peak frequencies, different quality factors, or different elasticity-to-viscosity ratios. The peak-frequency image of the blood-vessel network clearly displays two tiny elastomers in the region of interest; moreover, the color of the microelastomer on the left is green and represents a peak frequency of 0.8 MHz, and the color of the microelastomer on the

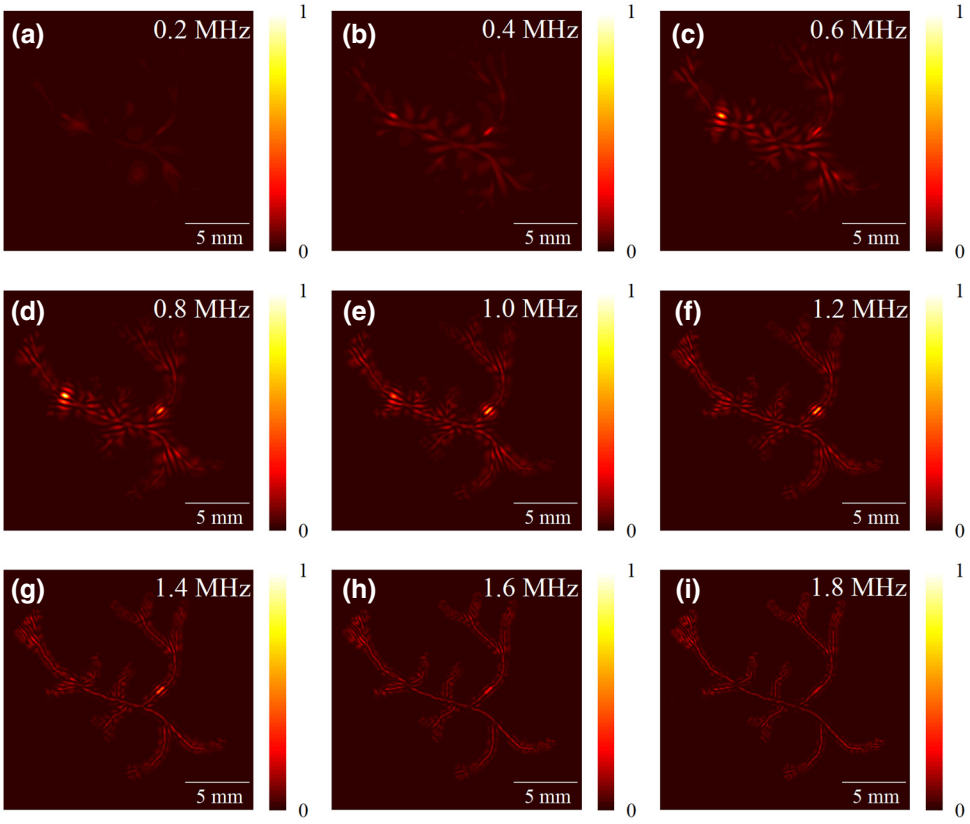

FIG. 7. Image sequence reconstructed from $s(\mathbf{r}_d,t,\omega_a)$. (a)–(i) Multispectral images with frequencies, ω_a, of 0.2, 0.4, 0.6, 0.8, 1.0, 1.2, 1.4, 1.6, and 1.8 MHz, respectively.

right is blue and represents a peak frequency of 1.2 MHz. Similarly, the quality-factor image shows that the color of the microelastomer on the left is blue, and its quality factor is approximately 3. The color of the microelastomer on the right is green, and its quality factor is approximately 2. However, in the elasticity-to-viscosity ratio image, both

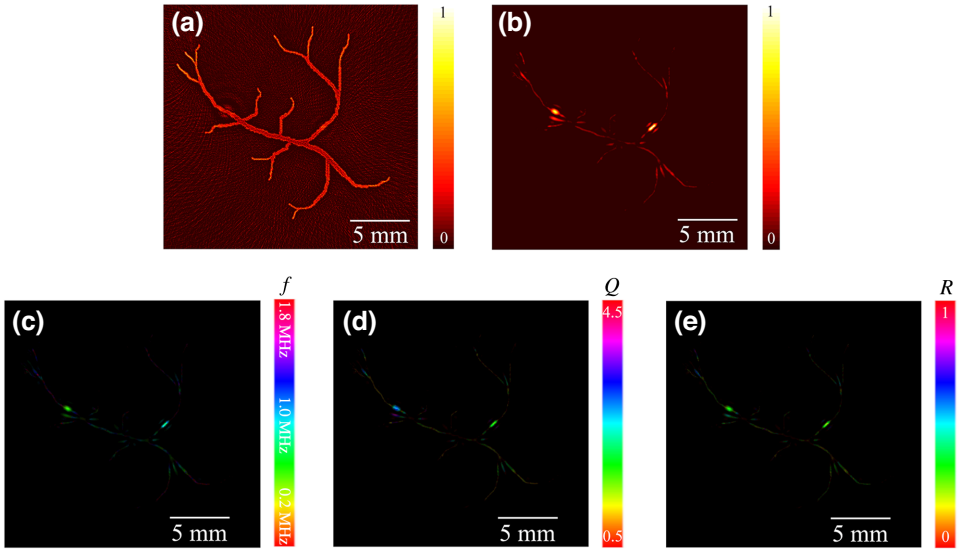

FIG. 8. Images of elastic segments in the blood-vessel network. (a) Reconstructed image using the delay-and-sum method. (b) Total-intensity image, $I(x,y)$, reconstructed using our proposed method. (c) Peak-frequency image, $\omega_p(x,y)$, of the region of interest encoded using HSV color space (hue, peak frequency; value, intensity). (d) Quality-factor image, $Q_p(x,y)$, of the region of interest encoded using HSV color space (hue, quality factor; value, intensity). (e) Elasticity-to-viscosity ratio image, $R_p(x,y)$, of the imaging region encoded using HSV color space (hue, elasticity-to-viscosity ratio; value, intensity).

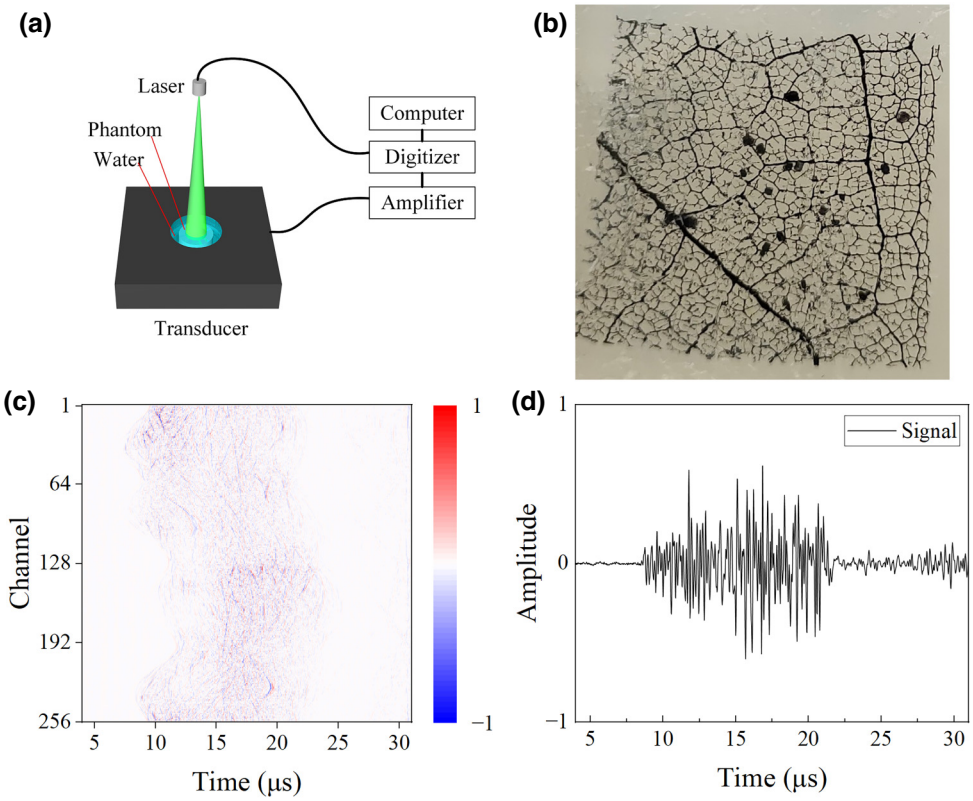

FIG. 9. Experimental setup for phantom and multichannel signals. (a) Schematic diagram of experimental setup. (b) Phantom consisting of dyed leaf and crushed eggshell fragments. (c) Waveform of the 256-channel detected signals. (d) Waveform of a typical detected signal.

the left and right microelastomers are depicted in green, indicating that they have similar ratios of elastic modulus to viscous modulus. Generally, the peak frequencies of elastomers in the elastograms are their eigenfrequencies. The frequencies, quality factors, and elasticity-to-viscosity ratios provided in Figs. 8(c)–8(e) are consistent with the eigenvibro frequencies, quality factors, and elasticity-to-viscosity ratios of the two microelastomers, correspondingly. This numerical experiment validates our proposed elastography method.

IV. EXPERIMENTS AND RESULTS

We also perform experiments to further evaluate our proposed method. We test a phantom, as shown in Fig. 9(b), consisting of a dyed leaf and crushed eggshell fragments. The dyed leaf and eggshell fragments are located in the same plane. The dyed leaf is inelastic, whereas the blackened eggshell fragments have high elasticity. A schematic of the experimental setup is shown in Fig. 9(a). A 532-nm Q-switched Nd:YAG laser with a pulse width of about 8 ns and a repetition rate of 10 Hz is used to illuminate the phantom. The laser beam has a pulse energy of approximately 30 mJ and a diameter of approximately 50 mm. The energy density is 1.53 mJ/cm^2, which is well within the laser safety limit according to the ANSI standard. A 256-element ring ultrasonic transducer array is used to collect the signals. The array has a central frequency of 5 MHz and a relative bandwidth of more than 60%. The photoacoustic signals are amplified by 54 dB and sampled with a sampling frequency of 50 MHz. Figure 9(c) shows the waveform of multichannel signals. Figure 9(d) displays the waveform of a typical signal.

Figure 10 shows the imaging results of the phantom. Figure 10(a) shows the conventional photoacoustic image of the phantom reconstructed with the delay-and-sum algorithm. This image clearly displays the structure of the leaf and the eggshell fragments. The intensity image, $I(x,y)$, in Fig. 10(b) is extracted from multispectral images, $A(x,y,\omega_a)$. The eggshell fragments have a much higher intensity than the leaf in image $I(x,y)$, indicating that the eggshell fragments have stronger elasticity. Figures 10(c)–10(e) show the peak-frequency image, the quality-factor image, and the elasticity-to-viscosity ratio image elastograms of the phantom. From Figs. 10(c)–10(e), eggshell fragments have high intensity, but the leaf is not observed in the elastogram. The elastic eggshell fragments are clearly shown in the images. The color of the eggshell fragments is yellow or green in Fig. 10(c),

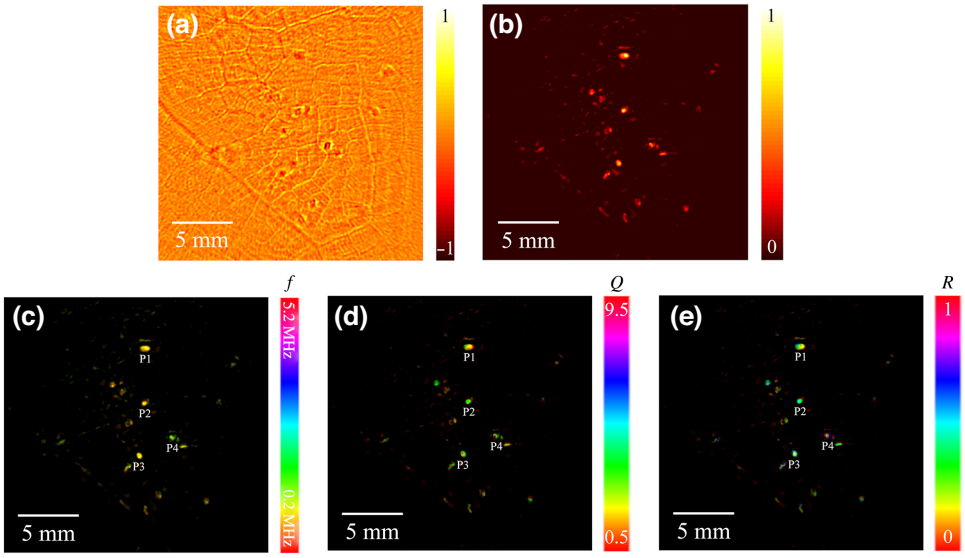

FIG. 10. Imaging the phantom of the dyed leaf mixed with the crushed eggshell fragments. (a) Conventional photoacoustic image of the phantom. (b) Intensity image, $I(x,y)$, reconstructed using our proposed method. (c) Peak-frequency image, $\omega_p(x,y)$, of the phantom encoded using HSV color space (hue, peak frequency; value, intensity). (d) Quality-factor image, $Q_p(x,y)$, of the phantom encoded using HSV color space (hue, quality factor; value, intensity). (e) Elasticity-to-viscosity ratio image, $R_p(x,y)$, of the phantom encoded using HSV color space (hue, elasticity-to-viscosity ratio; value, intensity).

indicating that the peak frequency of the eggshell fragments is approximately 1 MHz. Similarly, the color of the eggshell fragments is green or yellow in Fig. 10(d), indicating that their quality factors are distributed within the range of 1.5–3.5. Moreover, in Fig. 10(e), the color of the eggshell fragments is green or blue, indicating a distribution of normalized elasticity-to-viscosity ratios between 0.3 and 0.6. Four typical elastomers, P1–P4, are evidently displayed in the elastogram. P1–P4 have peak frequencies of 1.04, 0.85, 1.13, and 1.77 MHz, respectively, and their corresponding quality factors are 1.6, 3.5, 3.2, and 2.3, respectively. The normalized elasticity-to-viscosity ratios for P1–P4 are 0.27, 0.48, 0.58, and 0.66, respectively. In their elastograms, all eggshell fragments have similar peak frequencies, quality factors, and elasticity-to-viscosity ratios due to their similar sizes and hardness. Figure 10 shows that the elastogram obtained with our proposed method can show the intensity, peak-frequency, quality-factor, and elasticity-to-viscosity ratio information of microelastomers in a complex situation.

Figure 11 shows the imaging results of a silicone tube with an inner diameter of 0.8 mm and an outer diameter of 1.9 mm; the tube is filled with black ink and contains two pieces of glass capillary tubes with a diameter of 0.5 mm inserted inside, one located above and the other to the right of the silicone tube. Figures 11(a) and 11(b) show a photo of the silicone tube and a conventional photoacoustic image of the silicone tube reconstructed with the delay and sum algorithm, respectively. From Fig. 11(b), the black ink inside the tube is visible, but the capillary tubes are not well defined. Figures 11(c)–11(f) show the elastogram of the silicone tube, including the intensity image [$I(x,y)$], peak-frequency image [$\omega_p(x,y)$], quality-factor image [$Q_p(x,y)$], and elasticity-to-viscosity ratio image [$R_p(x,y)$]. The intensity image [Fig. 11(c)] is obtained from the multispectral images, $A(x,y,\omega_a)$, and shows the distribution of the total intensity of the eigenvibration energy in the region of interest. The intensity is higher in the upper and right sides of the tube, where the glass capillary tubes are inserted, indicating that the glass capillary tubes have stronger elasticity than the black ink. The distributions of the peak frequency, quality factor, and elasticity-to-viscosity ratio within the silicone tube are shown in Figs. 11(d)–11(f), respectively. In Figs. 11(d)–11(f), the color of the image indicates the value of the peak frequency, quality factor, or elasticity-to-viscosity ratio. The glass capillary tube located above the silicone tube has a peak frequency of 0.83 MHz, a quality factor of 4.5, and a normalized elasticity-to-viscosity ratio of 0.31, while the one to the right of the silicone tube has a peak frequency of 0.59 MHz, a quality factor of 4.9, and a normalized elasticity-to-viscosity ratio of 0.24. In Figs. 11(g)–11(i), both the low-elasticity silicone tube and the high-elasticity glass capillary tubes are appropriately imaged. Comparatively, the section without the glass capillary tube exhibits a lower frequency, a smaller quality factor, and a diminished elasticity-to-viscosity ratio compared to the section with the glass capillary tube. Overall, Fig. 11 demonstrates the capability of photoacoustic elastography to visualize the distribution of peak frequency and quality factor inside a small object, such as a silicone tube.

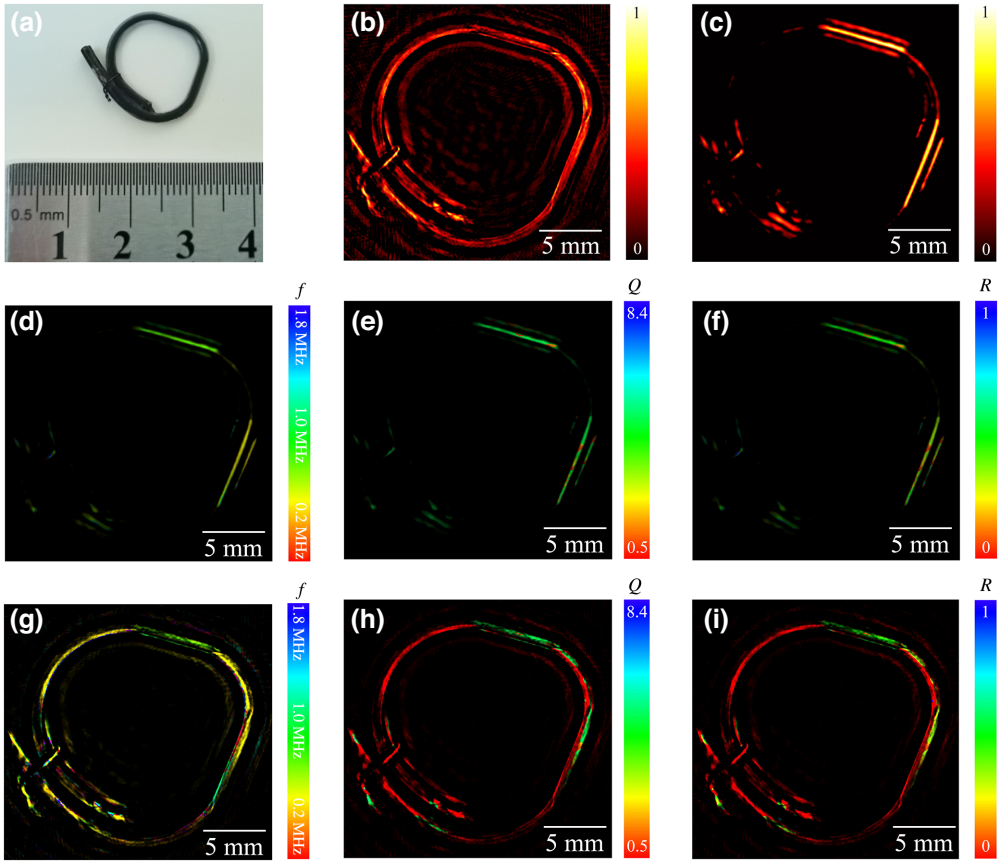

FIG. 11. Imaging a silicone tube. (a) Silicone tube with an inner diameter of 0.8 mm and an outer diameter of 1.9 mm, filled with black ink and containing two pieces of glass capillary tube with a diameter of 0.5 mm inserted inside. (b) Conventional photoacoustic image of the silicone tube. (c) Intensity image, $I(x,y)$, of the silicone tube. (d) Peak-frequency image, $\omega_p(x,y)$, of the silicone tube encoded using HSV color space (hue, peak frequency; value, intensity). (e) Quality-factor image, $Q_p(x,y)$, of the silicone tube encoded using HSV color space (hue, quality factor; value, intensity). (f) Elasticity-to-viscosity ratio image, $R_p(x,y)$, of the silicone tube encoded using HSV color space (hue, elasticity-to-viscosity ratio; value, intensity). (g) Peak-frequency image, $\omega_p(x,y)$, of the silicone tube encoded using HSV color space (hue, peak frequency; value, photoacoustic image). (h) Quality-factor image, $Q_p(x,y)$, of the silicone tube encoded using HSV color space (hue, quality factor; value, photoacoustic image). (i) Elasticity-to-viscosity ratio image, $R_p(x,y)$, of the phantom encoded using HSV color space (hue, elasticity-to-viscosity ratio; value, photoacoustic image).

V. CONCLUSION

In this study, we proposed photoacoustic multiacoustic spectral elastography based on the photoacoustic oscillation effect. After a laser pulse illuminated a light-absorbing elastomer, the elastomer continued vibrating and emitted ultrasound waves for a short time due to inertia. Weak damped transient waves emitted by the elastomer contained the elastic information. Our proposed method enhanced and decomposed eigenvibro signals by using a causal damped wavelet. Components from the eigenvibro signals via wavelet transform maintained spatial coherence and reached their own maxima at eigenvibration frequencies, and the other components were suppressed. Therefore, utilizing these components, we could reconstruct the elastogram of the region of interest. Both numerical simulations and phantom experiments effectively demonstrated the suitability of our proposed method.

In comparison with other elastography methods, our proposed elastography method has its own superiority. Optical coherence elastography can show microelastomers due to their high optical resolution. However, its imaging depth is only about 1 mm due to the limitation of strong optical diffusion in tissue. Therefore, optical coherence elastography is usually suitable for superficial tissue [50,51]. Ultrasound elastography can provide the elasticity of deep tissue, but it is often difficult to find small elastomers due to the low resolution and strong speckle [52,53]. However, benefitting from the photoacoustic effect and photoacoustic oscillation effect, our proposed elastography can obtain the elastogram of microelastomers in deep tissue under the interference of inelastic optical absorbers. Compared to pure optical elastography, our proposed method surpasses the optical diffraction limitation ($\sim$1 mm), allowing us to image the elastic properties of

deep tissue. It also has the capability to image microelastomers, which are elastic structures with dimensions comparable to or smaller than the wavelength of ultrasound, setting it apart from pure acoustic elastography.

Elastography for microelastomers in deep tissue can provide information about the mechanical properties of tissues, which can be an indicator of disease or injury [54–56]. Since lesions often develop from small to large and some diseases have weak early symptoms, tiny elastic changes can indicate the presence of lesions. Elastography for microelastomers in deep tissue can show subtle changes in tissue elasticity and help to differentiate between healthy and diseased tissue, identify the boundaries of tumors or lesions, and monitor the effectiveness of treatment. Additionally, it can aid in the detection of early-stage diseases, such as cancer, liver fibrosis, and lung disease, before they become clinically apparent. Therefore, our proposed elastography method for microelastomers in deep tissue has the potential to improve the accuracy of diagnosis and facilitate early intervention, which can ultimately lead to better patient outcomes.

ACKNOWLEDGMENT

This work was supported by the National Natural Science Foundation of China (Grants No. 12027808, No. 11834008, No. 11874217, and No. 81971629).

[1] L. V. Wang and S. Hu, Photoacoustic tomography: *In vivo* imaging from organelles to organs, Science **335**, 1458 (2012).

[2] L. V. Wang and J. Yao, A practical guide to photoacoustic tomography in the life sciences, Nat. Methods **13**, 627 (2016).

[3] C. Tian, M. Pei, K. Shen, S. Liu, Z. Hu, and T. Feng, Impact of System Factors on the Performance of Photoacoustic Tomography Scanners, Phys. Rev. Appl. **13**, 014001 (2020).

[4] G. Frigenti, L. Cavigli, A. Fernández-Bienes, F. Ratto, S. Centi, T. García-Fernández, G. Nunzi Conti, and S. Soria, Resonant Microbubble as a Microfluidic Stage for All-Optical Photoacoustic Sensing, Phys. Rev. Appl. **12**, 014062 (2019).

[5] Q.-B. Lu, T. Liu, L. Ding, M.-H. Lu, J. Zhu, and Y.-F. Chen, Probing the Spatial Impulse Response of Ultrahigh-Frequency Ultrasonic Transducers with Photoacoustic Waves, Phys. Rev. Appl. **14**, 034026 (2020).

[6] M. Zhang, Y. Chen, W. Xie, S. Wu, J. Liao, and Q. Cheng, Photoacoustic power azimuth spectrum for microvascular evaluation, Photoacoustics **22**, 100260 (2021).

[7] A. A. Plumb, N. T. Huynh, J. Guggenheim, E. Zhang, and P. Beard, Rapid volumetric photoacoustic tomographic imaging with a Fabry-Perot ultrasound sensor depicts peripheral arteries and microvascular vasomotor responses to thermal stimuli, Eur. Radiol. **28**, 1037 (2018).

[8] F. Yang, Z. Wang, W. Zhang, H. Ma, Z. Cheng, Y. Gu, H. Qiu, and S. Yang, Wide-field monitoring and real-time local recording of microvascular networks on small animals with a dual-raster-scanned photoacoustic microscope, J. Biophotonics **13**, e202000022 (2020).

[9] Ekaterina I. Galanzha, Yulian A. Menyaev, Aayire C. Yadem, Mustafa Sarimollaoglu, Mazen A. Juratli, Dmitry A. Nedosekin, Stephen R. Foster, Azemat Jamshidi-Parsian, Eric R. Siegel, Issam Makhoul, Laura F. Hutchins, James Y. Suen, Vladimir P. Zharov, *In vivo* liquid biopsy using cytophone platform for photoacoustic detection of circulating tumor cells in patients with melanoma, Sci. Transl. Med. **11**, eaat5857 (2019).

[10] Z. Wang, X. Zhen, P. K. Upputuri, Y. Jiang, J. Lau, M. Pramanik, K. Pu, and B. Xing, Redox-activatable and acid-enhanced nanotheranostics for second near-infrared photoacoustic tomography and combined photothermal tumor therapy, ACS Nano **13**, 5816 (2019).

[11] J. Ruan, Q. Yu, H. Cui, X. Qin, L. Qin, S. Chen, D. Niu, and C. Fan, A smart ROS/NIR dual-responsive melanin delivery platform for photoacoustic imaging-guided osteoarthritis therapy, Appl. Mater. Today **25**, 101216 (2021).

[12] C. Moore and J. V. Jokerst, Strategies for image-guided therapy, surgery, and drug delivery using photoacoustic imaging, Theranostics **9**, 1550 (2019).

[13] J. F. Greenleaf, M. Fatemi, and M. Insana, Selected methods for imaging elastic properties of biological tissues, Annu. Rev. Biomed. Eng. **5**, 57 (2003).

[14] R. Akhtar, M. J. Sherratt, J. K. Cruickshank, and B. Derby, Characterizing the elastic properties of tissues, Mater. Today **14**, 96 (2011).

[15] G.-Y. Li, Y. Jiang, Y. Zheng, W. Xu, Z. Zhang, and Y. Cao, Arterial stiffness probed by dynamic ultrasound elastography characterizes waveform of blood pressure, IEEE Trans. Med. Imaging **41**, 1510 (2022).

[16] A. K. Z. Tehrani, M. Ashikuzzaman, and H. Rivaz, Lateral strain imaging using self-supervised and physically inspired constraints in unsupervised regularized elastography, IEEE Trans. Med. Imaging **42**, 1462 (2022).

[17] W. Zeng, S. W. Gordon-Wylie, L. Tan, L. Solamen, M. D. J. McGarry, J. B. Weaver, and K. D. Paulsen, Nonlinear inversion MR elastography with low-frequency actuation, IEEE Trans. Med. Imaging **39**, 1775 (2020).

[18] H. Li, J. Poree, B. Chayer, M.-H. R. Cardinal, and G. Cloutier, Parameterized strain estimation for vascular ultrasound elastography with sparse representation, IEEE Trans. Med. Imaging **39**, 3788 (2020).

[19] R. Ahmed, J. Ye, S. A. Gerber, D. C. Linehan, and M. M. Doyley, Preclinical imaging using single track location shear wave elastography: Monitoring the progression of murine pancreatic tumor liver metastasis *in vivo*, IEEE Trans. Med. Imaging **39**, 2426 (2020).

[20] S. Goswami, R. Ahmed, S. Khan, M. M. Doyley, and S. A. McAleavey, Shear induced non-linear elasticity imaging: Elastography for compound deformations, IEEE Trans. Med. Imaging **39**, 3559 (2020).

[21] Qi Zeng, Mohammad Honarvar, Caitlin Schneider, Shahed Khan Mohammad, Julio Lobo, Emily H. T. Pang, Kirby T. Lau, Changhong Hu, James Jago, Siegfried R. Erb, Robert Rohling, Septimiu E. Salcudean, Three-dimensional multi-frequency shear wave absolute vibro-elastography

(3D S-WAVE) with a matrix array transducer: Implementation and preliminary *in vivo* study of the liver, IEEE Trans. Med. Imaging **40**, 648 (2021).

[22] P. N. T. Wells and H.-D. Liang, Medical ultrasound: Imaging of soft tissue strain and elasticity, J. R. Soc. Interface **8**, 1521 (2011).

[23] A. Sarvazyan, T. J. Hall, M. W. Urban, M. Fatemi, S. R. Aglyamov, and B. S. Garra, An overview of elastography-an emerging branch of medical imaging, Curr. Med. Imaging Rev. **7**, 255 (2011).

[24] M. Ducousso, E. Cuenca, M. Marmonier, L. Videau, F. Coulouvrat, and L. Berthe, Bulk Probing of Shock Wave Spatial Distribution in Opaque Solids by Ultrasonic Interaction, Phys. Rev. Appl. **15**, L051002 (2021).

[25] J. Abderezaei, W. Zhao, C. L. Grijalva, G. Fabris, S. Ji, K. Laksari, and M. Kurt, Nonlinear Dynamical Behavior of the Deep White Matter during Head Impact, Phys. Rev. Appl. **12**, 014058 (2019).

[26] D. Espíndola, S. Lee, and G. Pinton, Shear Shock Waves Observed in the Brain, Phys. Rev. Appl. **8**, 044024 (2017).

[27] M. Zheng, X. Liu, Y. Chen, H. Miao, R. Zhu, and G. Hu, Theory and Realization of Nonresonant Anisotropic Singly Polarized Solids Carrying Only Shear Waves, Phys. Rev. Appl. **12**, 014027 (2019).

[28] J. Yu, H. Guo, M. Han, F. Wang, A. Bouakaz, H. Zhang, and M. Wan, Transcranial Ultrasound Estimation of Viscoelasticity and Fluidity of the Soft Matter, Phys. Rev. Appl. **17**, 024001 (2022).

[29] P. Hai, Y. Zhou, L. Gong, and L. V. Wang, Quantitative photoacoustic elastography in humans, J. Biomed. Opt. **21**, 066011 (2016).

[30] P. Hai, Y. Zhou, L. Gong, and L. V. Wang, Photoacoustic elastography, Opt. Lett. **41**, 725 (2016).

[31] S. Du, Z. Chen, and D. Xing, Spectral interferometric depth-resolved photoacoustic viscoelasticity imaging, Opt. Lett. **46**, 1724 (2021).

[32] F. Yang, Z. Chen, and D. Xing, All-optical noncontact phase-domain photoacoustic elastography, Opt. Lett. **46**, 5063 (2021).

[33] Y. Yuan, X. Wen, B. Yuan, H. Xin, B. Fang, S. Yang, and K. Xiong, Photoacoustic remote sensing elastography, Opt. Lett. **48**, 2321 (2023).

[34] B. Audoin, Principles and advances in ultrafast photoacoustics; applications to imaging cell mechanics and to probing cell nanostructure, Photoacoustics **31**, 100496 (2023).

[35] Fernando Perez-Cota, Rafael Fuentes Dominguez, Salvatore La Cavera III, William Hardiman, Mengting Yao, Kerry Setchfield, Emilia Moradi, Shakila Naznin, Amanda Wright, Kevin Francis Webb, Alan Huett, Claire Friel, Virginie Sottile, Hany M Elsheikha, Richard Smith, Matt Clark, Picosecond ultrasonics for elasticity-based imaging and characterization of biological cells, J. Appl. Phys. **128**, 160902 (2020).

[36] L. Liu, L. Plawinski, M.-C. Durrieu, and B. Audoin, Label-free multi-parametric imaging of single cells: Dual picosecond optoacoustic microscopy, J. Biophotonics **12**, e201900045 (2019).

[37] X. Gao, C. Tao, X. Liu, and X. Wang, Photoacoustic eigen-spectrum from light-absorbing microspheres and its application in noncontact elasticity evaluation, Appl. Phys. Lett. **110**, 054101 (2017).

[38] T. Zhang, X. Liu, C. Tao, X. Xu, and X. Liu, Noncontact evaluation of full elastic constants of perovskite $MAPbBr_3$ via photoacoustic eigen-spectrum analysis in one test, Sci. Rep. **10**, 9994 (2020).

[39] F. Gao, X. Feng, and Y. Zheng, Photoacoustic elastic oscillation and characterization, Opt. Express **23**, 20617 (2015).

[40] H. Yang, T. Zhang, C. Tao, and X. Liu, Multispectral photoacoustic holography of elastomers from a bright background, Opt. Lett. **46**, 5071 (2021).

[41] J. D. Ferry, *Viscoelastic Properties of Polymers* (John Wiley & Sons, New York, 1980), 3rd ed.

[42] S. Rosat, P. Sailhac, and P. Gegout, A wavelet-based detection and characterization of damped transient waves occurring in geophysical time-series: Theory and application to the search for the translational oscillations of the inner core, Geophys. J. Int. **171**, 55 (2007).

[43] M. Mozaffarzadeh, A. Mahloojifar, M. Orooji, S. Adabi, and M. Nasiriavanaki, Double-stage delay multiply and sum beamforming algorithm: Application to linear-array photoacoustic imaging, IEEE Trans. Biomed. Eng. **65**, 31 (2018).

[44] X. Ma, C. Peng, J. Yuan, Q. Cheng, G. Xu, X. Wang, and P. L. Carson, Multiple delay and sum with enveloping beamforming algorithm for photoacoustic imaging, IEEE Trans. Med. Imaging **39**, 1812 (2020).

[45] M. Xu and L. V. Wang, Universal back-projection algorithm for photoacoustic computed tomography, Phys. Rev. E **71**, 016706 (2005).

[46] Q. Wang, Y. Shi, F. Yang, and S. Yang, Quantitative photoacoustic elasticity and viscosity imaging for cirrhosis detection, Appl. Phys. Lett. **112**, 211902 (2018).

[47] Y. Zhao, C. Chen, H. Liu, S. Yang, and D. Xing, Time-resolved photoacoustic measurement for evaluation of viscoelastic properties of biological tissues, Appl. Phys. Lett. **109**, 203702 (2016).

[48] B. E. Treeby and B. T. Cox, *K*-Wave: MATLAB toolbox for the simulation and reconstruction of photoacoustic wave fields, J. Biomed. Opt. **15**, 021314 (2010).

[49] B. E. Treeby, J. Jaros, and A. P. Rendell, Modeling nonlinear ultrasound propagation in heterogeneous media with power law absorption using a *K*-space pseudospectral method, J. Acoust. Soc. Am. **131**, 14 (2012).

[50] Mitchell A Kirby, Kanheng Zhou, John J Pitre, Liang Gao, David Li, Ivan Pelivanov, Shaozhen Song, Chunhui Li, Zhihong Huang, Tueng Shen, Ruikang Wang, Matthew O'Donnell, Spatial resolution in dynamic optical coherence elastography, J. Biomed. Opt. **24**, 1 (2019).

[51] V. Y. Zaitsev, A. L. Matveyev, L. A. Matveev, A. A. Sovetsky, M. S. Hepburn, A. Mowla, and B. F. Kennedy, Strain and elasticity imaging in compression optical coherence elastography: The two-decade perspective and recent advances, J. Biophotonics **14**, e202000257 (2021).

[52] R. Prado-Costa, J. Rebelo, J. Monteiro-Barroso, and A. S. Preto, Ultrasound elastography: Compression elastography

and shear-wave elastography in the assessment of tendon injury, Insights Imaging **9**, 791 (2018).

[53] A. Ozturk, J. R. Grajo, M. Dhyani, B. W. Anthony, and A. E. Samir, Principles of ultrasound elastography, Abdom. Radiol. **43**, 773 (2018).

[54] J.-M. Correas, A.-M. Tissier, A. Khairoune, V. Vassiliu, A. Méjean, O. Hélénon, R. Memo, and R. G. Barr, Prostate cancer: Diagnostic performance of real-time shear-wave elastography, Radiology **275**, 280 (2015).

[55] T. Miyagawa, M. Tsutsumi, T. Matsumura, N. Kawazoe, S. Ishikawa, T. Shimokama, N. Miyanaga, and H. Akaza, Real-time elastography for the diagnosis of prostate cancer: Evaluation of elastographic moving images, Jpn. J. Clin. Oncol. **39**, 394 (2009).

[56] L. Pallwein, M. Mitterberger, P. Struve, G. Pinggera, W. Horninger, G. Bartsch, F. Aigner, A. Lorenz, F. Pedross, and F. Frauscher, Real-time elastography for detecting prostate cancer: Preliminary experience, BJU Int. **100**, 42 (2007).